Large Eddy Simulation of Advancing Rotor for Near to Far Wake Assessment

D.-G. Caprace[1], S. Buffin[1], M. Duponcheel[1], P. Chatelain[1], G. Winckelmans[1]

[1] Institute of Mechanics, Materials and Civil Engineering, Université catholique de Louvain, 1348 Louvain-la-Neuve, Belgium

E-mail: denis-gabriel.caprace@uclouvain.be

43^{rd} European Rotorcraft Forum, Milan, 2017.

Abstract

The present work focuses on the Large Eddy Simulation of the wake flow behind an advancing rotor, to support the investigation of rotorcraft wake characteristics and decay mechanisms. A mixed Lagrangian-Eulerian Vortex Particle-Mesh (VPM) method was employed to simulate the near to far wake development of a four-bladed rotor. The rotor configuration was chosen to mimic the set-up of the high advance ratio experiment on an articulated rotor conducted at the University of Maryland in 2014. For an advance ratio of 0.41, results on trim control inputs are compared between the present simulations and the experiment. Then, the wake generation and development mechanisms are described (i) qualitatively in terms of vortex dynamics using rotor polar plots and 3D visualizations; (ii) quantitatively using classical integral diagnostics. A preliminary analysis shows that the strength of the emerging wake vortices increases over the first 30 diameter distance behind the rotor. This behavior is traced back to a longitudinal alignment of vorticity, driven by vortex stretching.

1. INTRODUCTION

It is a fact that, nowadays, airspace has reached an unprecedented level of utilization with the increase in air traffic over the last decades. The regions neighboring airports are often the most dangerous and the most regulated: with the convergence of many flights, possibly mixing various type of traffic (small and large aircraft, helicopters, etc.), the world biggest airport hubs reach saturation. In these airports, there is a strong demand of maximizing the utilization of runways by means of reducing the separation between successive craft. In the past decades, this demand has motivated much research effort which focused on aircraft wakes for the prediction of wake turbulence severity and the determination of safe reduced separation minima (see [1] for a recent review). The European Wake Vortex Re-categorisation (RECAT-EU) project and the application of Time-Based Separation (TBS) are examples which recently contributed to runway throughput augmentation, in the framework of the European project SESAR.

In comparison to their fixed-wing counterparts, investigations of rotorcraft wakes are quite scarce. The subject has however become important as demonstrated by a growing number of wake encounter incidents and accidents [2, 3]. Such occurrences often entail smaller airports where light aircraft are mixed with heavy rotorcraft. Incidentally, the most dangerous situations often imply the wake of rotorcraft which, from the regulation point of view, are submitted to vague separation rules and advised practices.

Unfortunately, the available studies, mostly numerical, are limited to the near wake, and far wake experimental investigations are almost nonexistent, at least for helicopter rotors. By essence, conventional free wake methods are inappropriate for far wake predictions due to their inviscid assumption [4, 5], and further advanced computational methods must be used. Detached Eddy Simulation was employed on hovering and advancing rotors and captured the near wake at high resolutions [6]. Other CFD methods for wake capturing usually use the vorticity-velocity form of the Navier-Stokes equation, like the Vorticity Transport Model [7]. Fully Lagrangian solvers were also employed for the computation of rotor wakes, with a blade representation using either lifting lines [8] or panel methods [9]. Domain decompositions were also developed in order to couple a Eulerian solver for the near body flow computation, and a Vortex Particle method for the

far field [10, 11, 12, 13]. To the authors knowledge, however, no published research has ever addressed rotorcraft far wakes with an objective of characterization and categorization.

Novel insights into the complex flow dynamics governing the development and the decay of rotorcraft wakes are thus necessary in order to predict appropriate safety margins, and eventually to develop tools to adapt procedures in very busy airspaces.

This work is concerned with the development of a numerical tool capable of accurately simulating the wake of a rotorcraft over large distances. In Section 2, we present a mixed Lagrangian-Eulerian computational method, called Vortex Particle-Mesh (VPM) method (see [14, 15] for recent applications), that we use for the Large Eddy Simulation (LES) of advancing rotors. Then, results of the simulations of a four-bladed rotor are presented. The studied configuration, which reproduces the experimental set-up by Berry and Chopra [16], is presented in Section 3.1. Section 3.2 presents a comparison between the experimental results and our simulations regarding trim. Finally, in Section 3.3, a preliminary analysis of the far wake of this rotor is presented.

2. METHOD

In this work, a state-of-the-art VPM method is employed. It relies on the vorticity-velocity ($\boldsymbol{\omega} - \mathbf{u}$) formulation of the Navier-Stokes equations for incompressible flows ($\nabla \cdot \mathbf{u} = 0$):

$$\frac{D\boldsymbol{\omega}}{Dt} = (\nabla \mathbf{u}) \cdot \boldsymbol{\omega} + \nu \nabla^2 \boldsymbol{\omega} \,, \tag{1}$$

where $\frac{D}{Dt} = \frac{\partial}{\partial t} + \mathbf{u} \cdot \nabla$ denotes the Lagrangian derivative and ν is the kinematic viscosity. Using a Helmholtz decomposition of the velocity field $\mathbf{u} = \mathbf{U}_\infty + \mathbf{u}_\omega$, one recovers $\mathbf{u}_\omega$ from the vorticity through the resolution of the Poisson equation

$$\nabla^2 \mathbf{u}_\omega = -\nabla \times \boldsymbol{\omega} \,. \tag{2}$$

Similarly to classical Vortex Particle methods, the advection term is handled in a Lagrangian fashion (akin to [17]). The flow is discretized using a set of particles characterized by a position $\mathbf{x}_p$ and a strength $\boldsymbol{\alpha}_p = \int_{V_p} \boldsymbol{\omega} d\mathbf{x}$, where V_p stands for the material volume associated to the particle. The evolution of the position and the strength of these vorticity carrying particles is recovered from the resolution of the following ODEs,

$$\frac{d\mathbf{x}_p}{dt} = \mathbf{u}(\mathbf{x}_p) \,, \tag{3}$$

$$\frac{d\boldsymbol{\alpha}_p}{dt} = \int_{V_p} \left((\boldsymbol{\omega} \cdot \nabla)\mathbf{u} + \nu \nabla^2 \boldsymbol{\omega} \right) d\mathbf{x} \,, \tag{4}$$

which are here solved using a third order Runge-Kutta scheme. We identify the role of the velocity field in the advection, and of the vortex stretching and diffusion terms for the evolution of vorticity.

In the present hybrid VPM method however, all the spatial differential operations are computed on an underlying mesh [18], thus in a Eulerian manner. The right-hand-side of Eq. (4) uses fourth-order finite differences; the turbulence Sub-Grid Scale model is implemented as in [19]. The Poisson solver for the velocity also exploits the Eulerian formulation and operates in Fourier space, which simultaneously allows for unbounded directions and inlet/outlet boundaries [20], in the context of a massively parallel implementation (here based on the PPM library [21]). High order interpolation schemes are used to recover information back and forth between the particles and the mesh.

In order to avoid particle clustering or depletion (a well known problem in VP methods), a redistribution operation occasionally resets the particles on a cartesian grid. Reprojection of the vorticity field is also periodically applied to maintain the solenoidal property of the vorticity field, which is otherwise not directly enforced by the solver. More details on these operators can be found in [22].

The VPM method thus benefits from the desirable properties of Lagrangian approaches known as almost non-dispersive, and it also waives the classical CFL condition, thus allowing for larger time steps.

The rotor blades are not fully resolved in the present research; their coarse scale aerodynamics are rather accounted for through an Immersed Lifting Line (ILL) method [23]. Based on the instantaneous velocity and angle of attack of every blade segment, a 3^{rd} generation Leishman-Beddoes Dynamic Stall (DS) model (explained in [24]) is used to compute the lift and drag produced by the airfoil, thus aiming at a better representation of the complex unsteady aerodynamics. Then, under the assumption of quasi-steady flow around the airfoil, the circulation around the

local 2D airfoil is recovered from

$$\mathbf{L} = \rho \mathbf{V}_{\text{rel}} \times \mathbf{\Gamma} \,, \tag{5}$$

where $\mathbf{L}$ is the lift per unit span of the segment, $\mathbf{V}_{\text{rel}}$ is the relative flow velocity and $\mathbf{\Gamma}$ is the circulation. In the flow, the blade segments are then represented by a set of equivalent bound vorticity particles. The shed vorticity, which is deduced from the variation of the bound vorticity, is released in the bulk flow through new vorticity carrying particles and then merged with the pre-existing flow particles.

Unlike an Actuator Line technique [25], the ILL method thus preserves the Lagrangian character of the overall formulation. However, the shed structures do not account for drag, in a fashion akin to Vortex Lattice or Free Wake methods.

The rigid blade flapping motion is captured through a loose coupling of the flow solver with the multi-body integrator ROBOTRAN [26]. The latter uses symbolic generation to establish the equations of the direct dynamics of a model (here, the rotor). This approach enables the efficient solving of the dynamics of complex multi-body systems such as the complete mechanisms of a rotor hub, provided that the blade aerodynamics forces can be recovered from the flow solver. In the current loosely coupled implementation, ROBOTRAN uses a separate time integrator to advance the state of the multi-body system from the forces obtained by the flow solver at each time step. The positions of the lifting bodies are then updated in the flow simulation and the process is iterated.

In the present case, a rather simple rotor model is used. It consists of a rotor shaft rotating at a prescribed angular velocity. The blades are connected to the shaft at a certain inner rotor radius radius R_i from the center of revolution, and have two degrees of freedom, respectively for flapping and pitching. The blades pitching motion is prescribed by a close loop controller in order to cancel the pitching and rolling moments of the rotor measured at the hub center, using classical cyclic controls (θ_{1c} and θ_{1s}). The collective (θ_0) can also be dynamically adapted to maintain a given thrust coefficient C_T for the rotor. The aerodynamic and inertial efforts applied on each blade thus result in the their flapping angle β, integrated in time.

In the remainder of the article, the VPM method coupled to ROBOTRAN is simply referred to as *VPM*.

3. RESULTS

In this section, we study the coarse-scale aerodynamics of the blades and then the large-scale wake behavior of an advancing rotor.

3.1. Rotor configuration

The configuration considered here reproduces the experimental set-up by Berry, Chopra [16], and Bowen-Davis [27] who studied an articulated four-bladed rotor under moderate to very high advance ratios, and for various tilt angles of the rotor shaft. The rotor and blade properties are summarized in Table 1.

Rotor radius, $R\,[m]$	0.849
Blade chord, $c\,[m]$	0.080
Solidity, s	0.120
Airfoil	NACA0012
Hinge offset, $[\%R]$	6.3%
Root cut-out, $[\%R]$	22.5%
Twist	untwisted
Sweep	unswept
Blade mass, $m_0\,[kg/m]$	0.347
Flap inertia, $I_\beta\,[kg\,m^2]$	0.058

Table 1: Rotor and blade properties from [27].

In this work, we only consider the case of an advance ratio of $\mu = \frac{U_\infty}{R\Omega} = 0.41$. This was the lowest ratio available from the experiment, but we assume it is still representative of a classical helicopter in high speed forward flight. For the selected rotor angular velocity $\Omega = 600\,[RPM]$, this corresponds to a Reynolds number of $Re_c = 4\,10^5$ at blade tip. Aerodynamic polars from [28] were used to tune the static coefficients of the DS model, while the standard values (summarized in [24]) are taken for the coefficients related to the dynamics.

We focus on two specific geometries for our simulations. The first one, for which we present the results in Section 3.2, has a rotor shaft which is perpendicular to the free stream velocity in order to exactly reproduce one of the experiments. The second geometry has the main rotor shaft tilted forward (nose down) to mimic the attitude of an advancing rotorcraft. The results of that case are presented in Section 3.3.

At this point, we should also recall that the aerodynamics of the rotor hub and of the mast were not taken into account in the model. Our method is also incompressible: this is compatible with the reference experiment for which the max-

imum blade tip Mach number would be around 0.2.

3.2. Rotor trim comparison

A first set of short-domain simulations is performed as a step toward the validation of our model against the experiment. Simulations are run for different values of the collective control θ_0, and the cyclic controls θ_{1c} and θ_{1s} are adapted in order to trim the rotor by cancelling the pitching and rolling moments at the hub. Two spatial resolutions are used: the coarse one corresponds to 32 particles per rotor radius, and the fine resolution to 64. The computational domain has unbounded boundary conditions in the two lateral directions. The inflow is located at $1D$ from the rotor hub, and the outflow is at $2D$.

Based on the thrust coefficient C_T and the cyclic control angles for trim θ_{1c} and θ_{1s}, a comparison between the experiment and the simulations is presented in Fig. 1. Data from the University of Maryland Advanced Rotorcraft Code (UMARC) are also presented. This model uses a flexible beam representation of the blades coupled to a lifting line free wake approach for the aerodynamics [29].

The Thrust coefficient is reasonably well captured around 0°. However, the slope of the curve is a bit underestimated by VPM, possibly due to the polar mismatches, or a poor prediction of the dynamic stall model. The refinement has only a small influence on the results, which is positive regarding the converged status of the simulations.

The slopes of the lateral cyclic (θ_{1c}) and longitudinal cyclic (θ_{1s}) curves at trim are correctly captured, while the values remain underestimated for θ_{1c} and overestimated for θ_{1s}. The non zero value measured at $\theta_0 = 0$ is most likely due to the hub and mast wake interacting with the blades.

Clearly, a more thorough analysis would be required to validate the current method in various cases, including hover and lower advance ratios. However, we consider the tool as ready for a preliminary analysis of far wake of such a rotor.

3.3. Extended wake simulation

The spatial development of the wake of the four-bladed rotor described in Section 3.1 is computed in one simulation with an extended computational domain. The rotor operates in the same conditions as above, except that the rotor shaft is here tilted nose down by 4°. Once again, the cyclic controls θ_{1c} and θ_{1s} are adapted in order to trim the rotor by cancelling the pitching and rolling moments at the hub. The collective is here also adapted in order to maintain a constant value of $C_T = 0.015$.

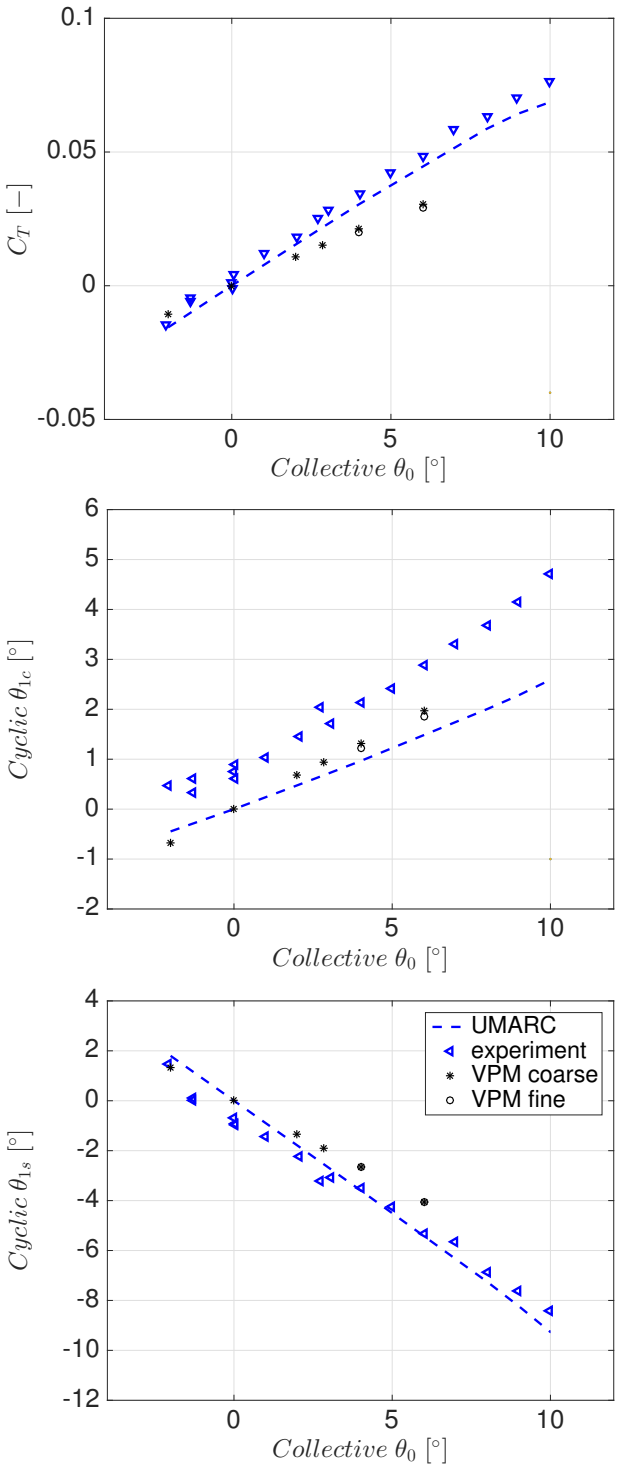

Figure 1: VPM simulation results for various angles of the collective, together with experimental results and UMARC simulations: thrust coefficient (top) and cyclic input controls for trim (center and bottom). [27]

The spatial resolution employed correspond to the refined case presented above (i.e., 64 particles per rotor radius). The computational domain has unbounded boundary conditions in the lateral directions. The inflow is located at $1.5\,D$ from the rotor hub, and the outflow is at $30.5\,D$ in an attempt to capture the complex transition from the near wake to a fully developed turbulent far wake.

The results presented below were obtained from a simulation run on 1024 processors for 24 hours. This corresponds to 2 convective times T_c, where $T_c = L/U_\infty = 32D/U_\infty$.

3.3.1. Rotor aerodynamics

First, we focus on the rotor operating conditions and on the mechanisms of near wake development. When trim conditions are achieved, we obtain the following control angles: $\theta_0 = 4.96°$, $\theta_{1c} = 0.62°$ and $\theta_{1s} = 2.90°$. It must be noted that the resulting blade motion leads to zero first harmonic flapping at the blade root, which confirms that the rotor is trimmed. The mean flapping angle is around $\beta = 1.9°$.

Obviously, the vorticity forming the early state of the wake strongly reflects the periodic sollicitations undergone by the rotor blades. The polar representation of the angle of attack (AoA, Fig. 2), the lift distribution (C_l^*, Fig. 3), and the blade circulation distribution (Γ, Fig. 4) on the rotor disk will help shed some light on the vorticity generation mechanism in the near wake.

The mean lift coefficient C_L experienced by one entire blade over one revolution is

$$C_L = \frac{1}{2\pi}\int_0^{2\pi}\int_0^R \frac{l(r,\psi)}{\frac{1}{2}\rho U_\infty^2 S}\,dr\,d\psi\,,$$

where l is the lift per unit span of the lifting line, and $S = \pi R^2$. Note that, in the present simulation, $C_L = 0.09$. For the sake of clear polar presentation, we define

$$C_l^* = \frac{1}{2\pi}\frac{l}{\frac{1}{2}\rho U_\infty^2 r}\,.$$

As a result, C_L is obtained by a classical polar integration of C_l^* shown on Fig. 3,

$$C_L = \frac{1}{S}\int_0^{2\pi}\int_0^R C_l^*\,r\,dr\,d\psi\,.$$

Clearly visible on the lift polar plot are the Blade Vortex Interactions (BVI) on the advancing side. The first, upstream most interaction divides the rotor into two regions: a fore region with high loadings and an aft region with lower loadings. This suggests that this interaction dramatically reduces the intensity of the crossing tip vortex as the blade sheds oppositely signed vorticity onto the passing vortex (as observed by [30] during perpendicular BVI). Subsequent BVIs

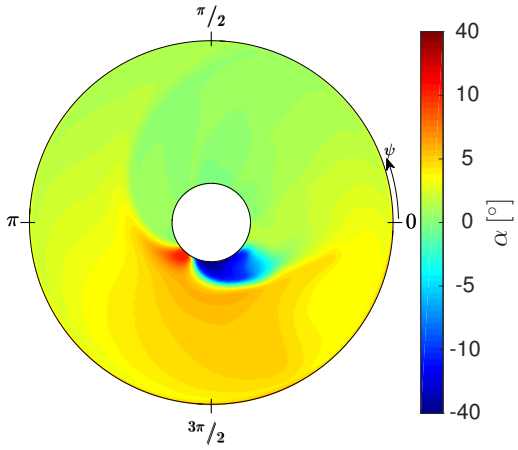

Figure 2: Angle of Attack over one rotor revolution.

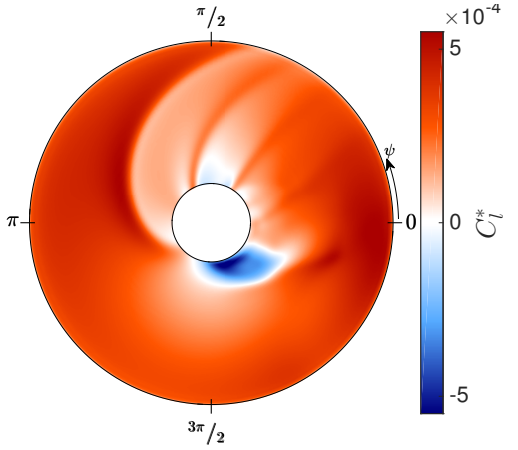

Figure 3: Lift produced by one blade over one rotor revolution.

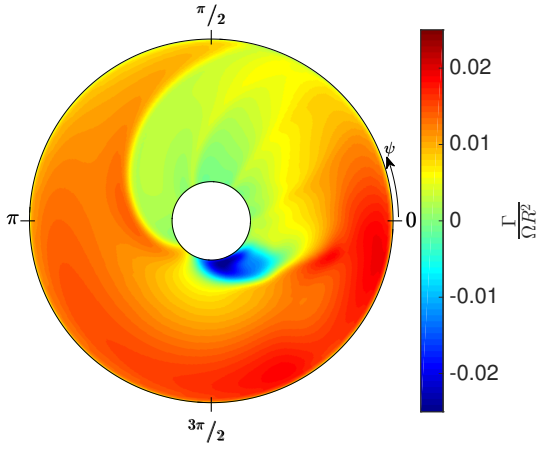

Figure 4: Blade circulation over one rotor revolution.

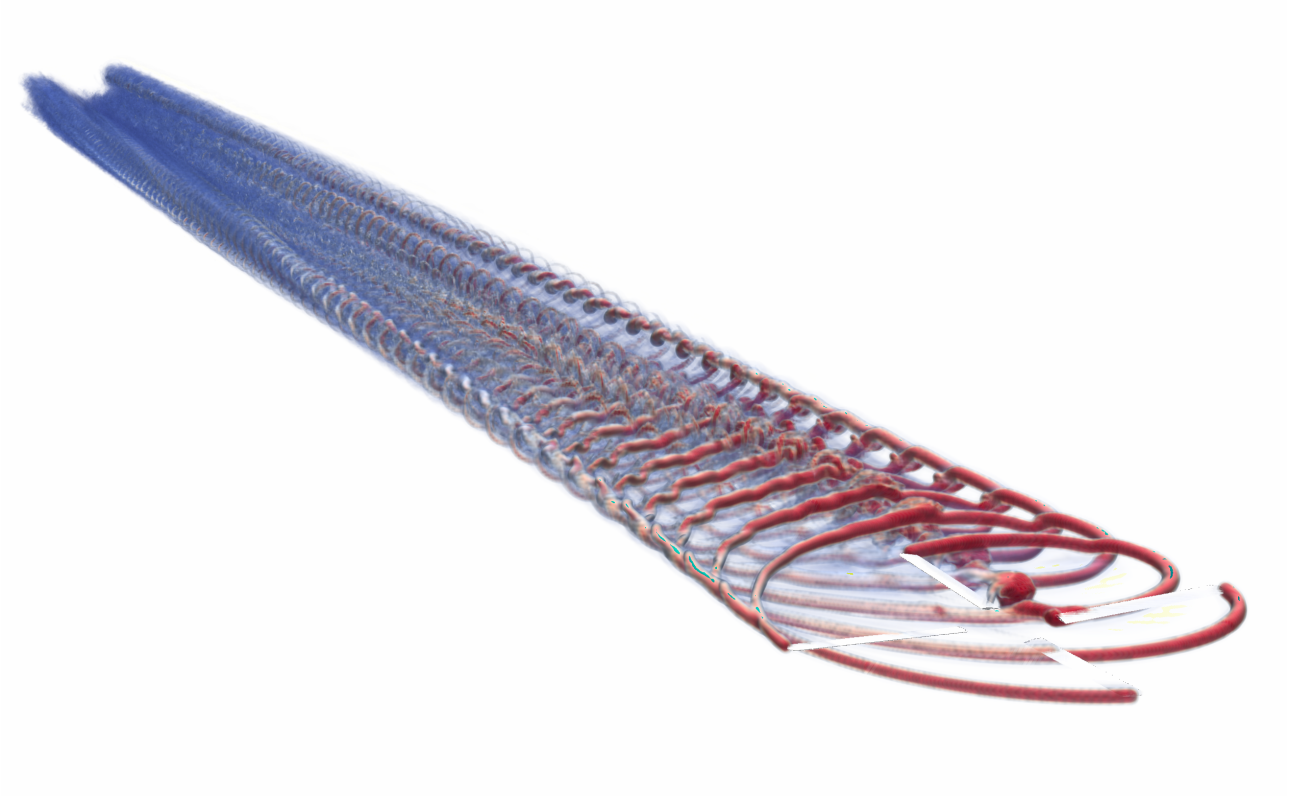

Figure 5: Volume rendering of the vorticity magnitude in the wake of the four-bladed rotor, over 30 rotor diameters.

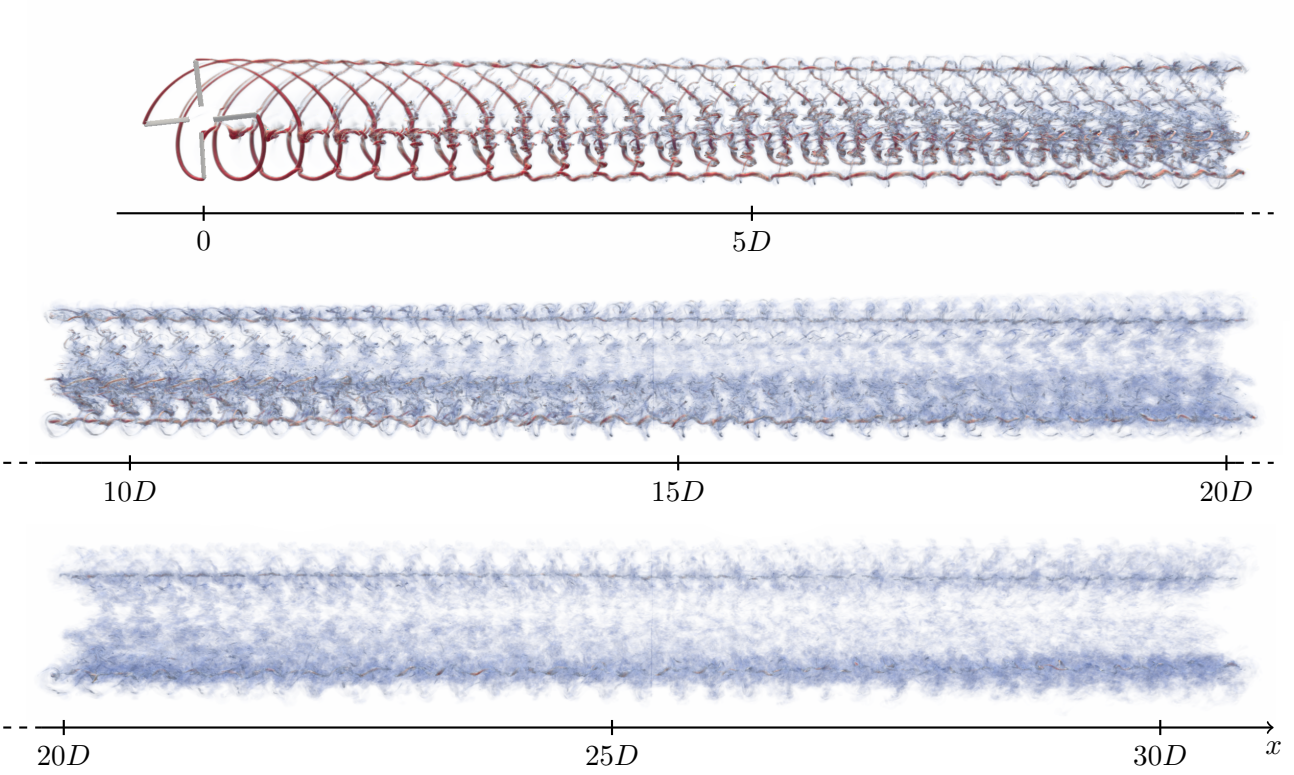

Figure 6: Near to far wake of the rotor, from the initial vortex generation to the roll-up and the establishment of a mainly turbulent wake.

appear to be weaker as the blade-vortex offset distance increases due to induced velocities. Still, these events, together with the overall induced velocity field in the rotor plane, are sufficient to generate an area of slight downward forces close to the hub.

The lift appears to be mainly produced in the fore part of the rotor on the advancing side, and in the aft part (around $\psi = 0$) where the blades are less subjected to interactions because they pass above the tip vortex paths.

On the retreating side, the blades experience a more homogeneous loading than on the advancing side, due to the absence of BVI. Yet, close to the hub, a sudden AoA increase is visible (up to 12°), followed by a sharp drop in the reverse flow region; the airfoil is not visiting completely adverse conditions, though. The circulation and lift respond rather smoothly in that region, indicating that dynamic stall might occur with a limited severity, but the delay in lift and circulation development consequently expand the affected area toward the rear of the disk.

It is clear that predictions in that region strongly depend on the dynamic stall model. Due to the proximity to the center of revolution, we expect a limited impact of the DS model uncertainty on the trim parameters. The circulation, however, is affected and the strong shedding events triggered by sudden circulation changes might be more sensitive to the DS behavior.

On average, the blade circulation has a higher value on the retreating side; this is to be correlated with a combination of smaller blade relative velocities and a roughly similar lift production. The strong circulation gradient in the outboard part of the disk hints at more intense tip vortices than those produced on the advancing side. From the polar plot of Γ, one can identify two types of features being shed in the near wake:

- at a certain azimuth, the vorticity shed from the spanwise variation of the blade circulation. The tip vortices best exemplify this type of shedding mechanism, as they result from the sharp drop in circulation at the tip;
- at a certain radius, the vorticity shed due to the temporal variation of the circulation. Dynamic stall, and more generally any rapid variation of the circulation will be the source of a shed vortex.

3.3.2. 3D wake development

Fig. 5 shows a 3D vorticity visualization by volume rendering of the wake, and Fig. 6 presents its whole extent from the top, cut in three panels. It can be seen that the "young" blade tip vortices are travelling on cycloidal paths, but are strongly disturbed by BVI and vortex-vortex interactions. As expected, tip vortices are more intense on the retreating side than on the advancing side. However, vortex mergers occur on the advancing side, which lead to an emerging, intense wake vortex; on the other side, reconnection events of the successive tip vortices also produce a single flow-aligned vortex. As a result, a globally dominating two-vortex system (2-VS) eventually governs the wake roll-up, with wake vortex cores apparently in a helical shape.

The merging and reconnection operations are also propitious to the generation of turbulence. In the inboard part of the wake, we observe crossing transverse structures originating in the blade tip vortices shed in the fore and aft part of the revolution. These are subject to stretching under the influence of the forming 2-VS; instabilities are triggered by these opposite sign and different intensity vortices interacting with each other. Finally, breakdown and transition to turbulence occur.

Complex vortical structures shed from the reverse flow region of the rotor also travel along the wake, and strongly interact with the nearby tip vortices produced during the aft part of the revolution. These disturbances propagates and contribute to a rapid development of turbulence, too.

The hub wake region (behind the rotor hub) should also be largely affected by the wake generated by the rotor hub himself, which is not represented here. It was recently observed by [31] that velocity in that region bears high harmonics of the rotor revolution frequency, from which we can expect the rapid development of a whole turbulent spectrum. The body wake behind the fuselage and the tail rotor are also important sources of turbulence which would further accelerate the transition and homogenization the wake.

3.3.3. Slice statistics

Statistics are monitored in six vertical slices distributed over 30 rotor diameters downstream of the rotor. First, we characterize the wake in terms of mean axial vorticity $\bar{\omega}_x$ (Fig. 7), averaged in time over 15 rotor revolutions.

The 2-VS can be seen as early as two diameters

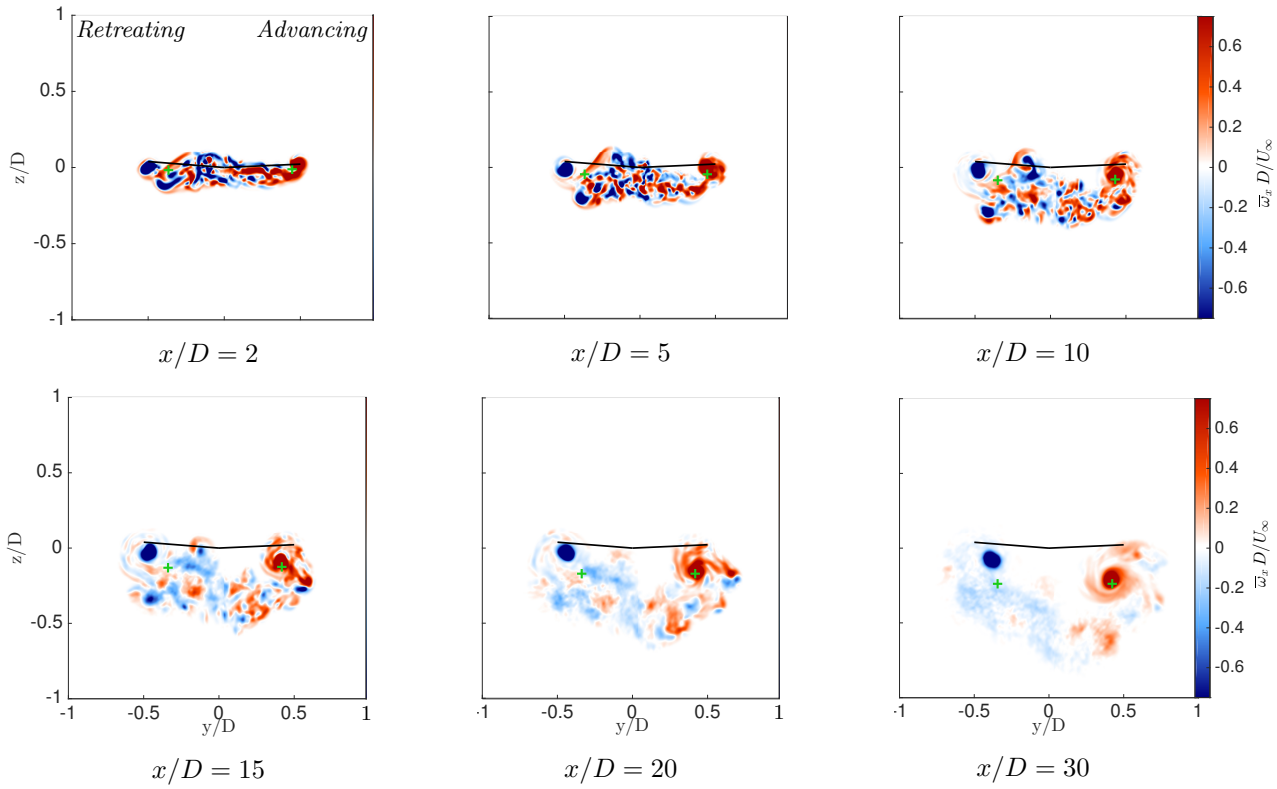

Figure 7: Evolution of the time-averaged axial vorticity in transverse slices at various stations along the wake. The (+) signs locate the vorticity centroid over each half plane.

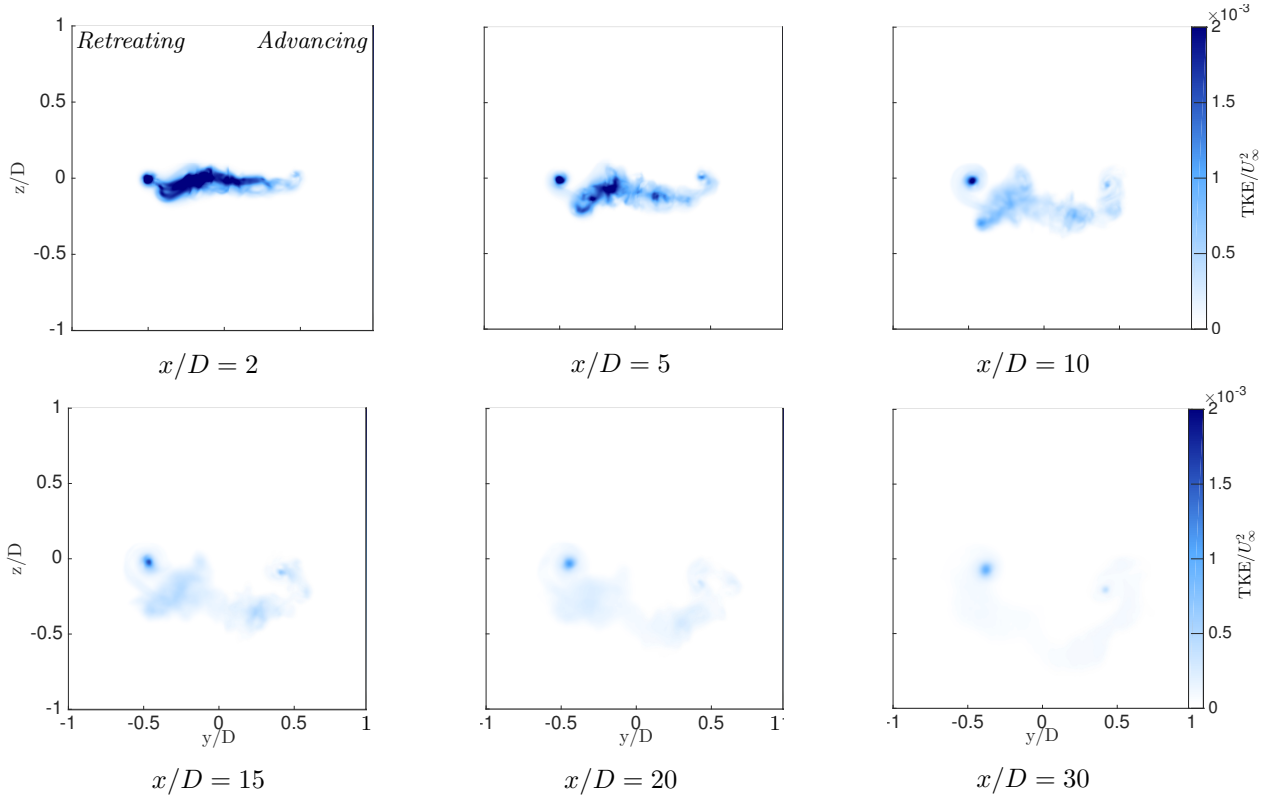

Figure 8: Evolution of the turbulent kinetic energy in transverse slices at various stations along the wake.

behind of the rotor. The vorticity in the cores remains visible far downstream, whereas the vorticity located in between the two main vortices tends to smear. This is due to the interactions between vortices of different size and strength, as seen in the 3D visualization, and here also visible through the presence of patches of opposite sign (even on the time average flow). After $20\,D$ though, the flow becomes more homogeneous, with large turbulent patches of same-sign vorticity.

The vortex core originating from the advancing side appears to travel downwards at a higher velocity than that of the retreating side. This, however, must not be interpreted as an imbalance in the rotor wake, as will be explained below through the computation of the angular impulse.

The turbulent kinetic energy (TKE) is also monitored (Fig. 8). Areas where the TKE is important (and is then also dissipated) are mainly located:

- close to the center of the main wake vortices (2-VS). It can be explained by the blade tip vortices merging and reconnections (resp. on the advancing and retreating side) generating turbulence which is progressively diffused.
- in the area downstream of the reverse flow region. As already noticed, the intense shedding occurring in that zone triggers strong interactions with the surrounding (more coherent) vortices, with the fast increase in turbulence as a result. This process contributes to the homogenization of the mean flow.

Clearly, the missing elements in the simulation (with respect to an actual rotorcraft, i.e. the fuselage, the hub, the tail rotor, etc.) would result in an even broader high TKE zone in the wake.

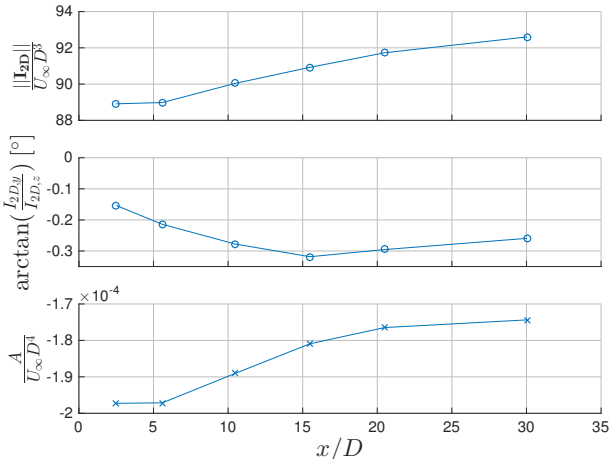

Figure 9: Impulse and angular impulse at different stations in the wake.

3.3.4. Wake integral diagnostics

The evolution and decay of the emerging 2-VS is now characterized in terms of integral quantities. The diagnostics presented here, and their interpretation in terms of device forces and moments, strictly hold for a purely two dimensional mean flow, which is obviously not the case close to the rotor. However, this approximation improves when the wake reaches a fully rolled-up and developed state.

Based on the mean axial vorticity field, we compute the 2D linear impulse $\mathbf{I}$ and angular impulse A on every slice

$$\mathbf{I}_{2D} = \int_{-\infty}^{\infty}\int_{-\infty}^{\infty} \mathbf{x} \wedge \bar{\omega}_x \, dy \, dz,$$

$$A = \int_{-\infty}^{\infty}\int_{-\infty}^{\infty} \mathbf{x} \wedge (\mathbf{x} \wedge \bar{\omega}_x) \; dydz;$$

the former is the signature of lift and side forces, the latter is the signature of the rolling moment. The results (Fig. 9) show that the linear impulse increases, hinting at a rather non-intuitive process discussed here under.

In spite of the absence of drag shed by the blades (purely lifting line model), one can verify that the wake is indeed balanced in terms of moments: the angular impulse A is close to zero and the linear impulse $\mathbf{I}$ vector is mostly vertical (it is tilted by maximum 0.3°).

The 2D circulation distribution is defined as

$$\Gamma(y) = \int_{-\infty}^{y}\int_{-\infty}^{\infty} -\bar{\omega}_x(y', z') \, dz' \, dy'.$$

It is an image of how the shed vorticity evolves and spreads out in the wake.

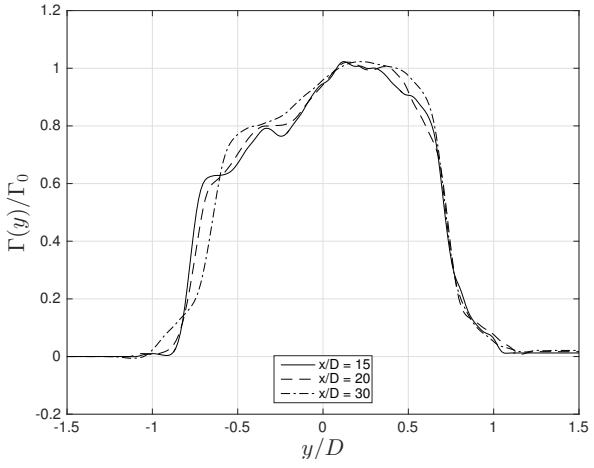

Figure 10: Circulation distribution across the slices.

Classically, it remains symmetrical for a wing during the roll-up process, but this is not the case for a rotor, as seen in Fig. 10. The maximum circulation shifts toward the advancing side, indicating that vorticity spreads more laterally on the retreating side.

$\Gamma(y)$ is to be correlated with the vorticity production and roll-up mechanisms on the rotor disk. The retreating side vortex has a strong vortex core generated by the reconnection of blade tip vortices, and is also dominated by a negative axial vorticity component originating in the structures shed in the reverse flow region and the subsequent interactions. The slope of the wake circulation is therefore moderate on that side. On the advancing side, however, interactions of vortices seem to induce a depletion of axial vorticity in the inboard part of the wake (also visible in Fig. 6 as from $x = 15D$), while feeding the main vortex.

A smoothing of the curve is also observed further downstream, once again under the influence of turbulence.

Similarly to aircraft wakes, we define the circulation over a half plane Γ_0. This quantity encompasses the circulation of one vortex of the 2-VS, and corresponds to the circulation distribution evaluated at the center of the wake y_0, $\Gamma_0 = \Gamma(y_0)$. Unlike aircraft wakes though, the definition of y_0 is not straightforward because the wake is not symmetric. As there is no angular momentum in the wake, we can assume that the wake mid plane remains vertical (i.e. along z), and we hence define the center location y_0 to satisfy the following relation:

$$\int_{-\infty}^{y_0} \Gamma(y)\, dy = \int_{y_0}^{\infty} \Gamma(y)\, dy.$$

The vortex spacing is then

$$b_0 = \frac{1}{\Gamma_0} \int_{-\infty}^{\infty} \int_{-\infty}^{\infty} -\bar{\omega}_x(y,z)\, y\, dydz.$$

The results from the simulations (Fig. 11) show a contraction of the 2-VS in the beginning, with a significant increase in $|\Gamma_0|$. The spacing b_0 tends to stabilize at around 76% of the rotor diameter, a value which is remarkably close to the classical elliptical wing configuration (for which $b_0 = \frac{\pi}{4} = 0.785$).

The vorticity centroids, computed on each half plane, are displayed on Fig. 7 to materialize the trajectory of the 2-VS, confirming the non-rotating behavior of the wake along the x-axis, and indicating that the contraction is more visible on the retreating side.

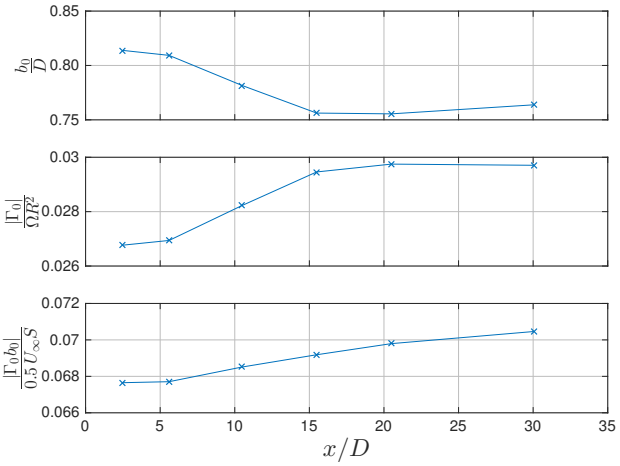

Figure 11: Wake vortex intensity Γ_0, spacing b_0 and their product, at different stations in the wake.

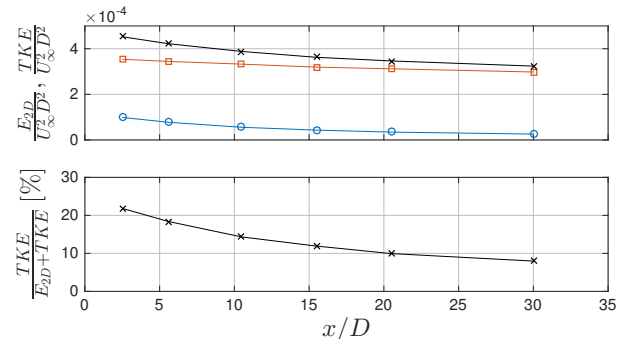

Figure 12: Kinetic energy of the cross stream E_{2D} (□), TKE (○) and their sum (×) integrated over 2D slices, at different stations in the wake.

Finally, we remind that the product $\Gamma_0\, b_0$ is related to the mean generated lift through $L = \rho\, U_\infty\, \Gamma_0\, b_0$. This quantity remains constant during the roll-up behind a simple wing. Surprisingly, the product is here rising as from $x = 5D$ and tends to reach a plateau after $x = 30D$ (same behavior as for **I**).

As a hypothesis, this could be caused by the alignment of transverse vorticity (ω_y, ω_z) in the flow direction, under the influence of stretching. The transverse structures highlighted in the previous section, which are specific to rotorcraft applications, seem to generate axial vorticity components during their interactions, thus increasing the 2D linear impulse measured in slices. The stabilization of the curve initiated around $20D$ possibly indicates the end of the transverse vorticity alignment process, and the establishment of the fully developed wake.

This establishment is confirmed by the fact that the kinetic energy of the cross flow $E_{2D} = \frac{\bar{v}^2+\bar{w}^2}{2}$ also reaches a plateau (Fig. 12). We note that, in the early state of the wake, the TKE amounts to a significant part of the total energy $E_{2D} + TKE$, but rapidly drops and stabilizes at around 8%. This is remarkably similar to the value of 8.1% reported in [32] for the 2-VS emanating from an elliptical wing, at equilibrium.

The vorticity alignment hypothesis is strengthened by the computation of the mean stretching term (Fig. 13): after $x = 5D$, the stretching term integrated over a half plane is negative on the retreating side and positive on the advancing side. As a result, negative and positive streamwise vorticities are respectively injected in the 2-VS, thus increasing Γ_0, on the one hand. On the other, the vortex spacing b_0 is sensitive to the locations of high stretching. Besides, the intensity of stretching decreases as from $x = 10D$ and almost reaches zero at $x = 30D$. This is consistent with the stabilization of the $\Gamma_0\, b_0$ curve.

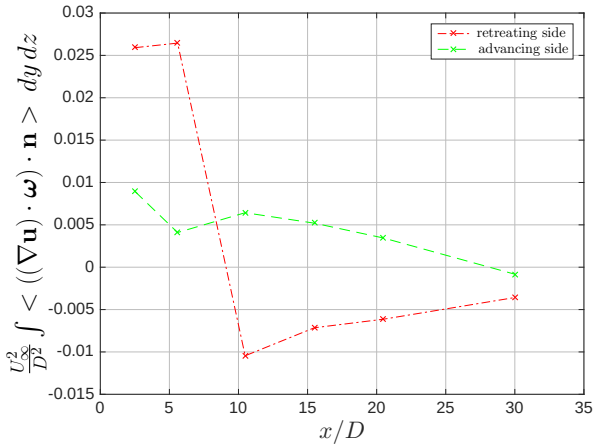

Figure 13: Mean vortex stretching contribution to axial vorticity, integrated over a half plane.

To finish with this preliminary analysis, the present 30 diameter long simulation does not indicate a sudden onset of wake decay. The establishment of a fully developed and turbulent wake flow has however been reached at the end of the simulation domain, after the transverse vorticity alignment process. Notice that, from that point on, one can then define the mean 2D 2-VS of the wake, with stabilized values of Γ_0 and b_0. For further distances downstream, this system should most likely behave like a standard 2-VS at equilibrium (like those studied in [32]).

It should be taken into consideration that this simulation used a rather simple rotor model. The rotor hub and mast, which are missing here, are likely to accelerate the mixing of the flow. Therefore, the fully developed state (i.e. the plateau on Γ_0 and b_0) might be reached earlier.

4. CONCLUSION & PERSPECTIVES

A Vortex Particle-Mesh method coupled to a multi-body solver has been briefly presented. It solves the Navier-Stokes equations in the vorticity-velocity form, using a hybridized Lagrangian-Eulerian formalism and subgrid scale modeling.

The overall method was tested against a reference experiment of a four-bladed rotor in a wind tunnel, at an advance ratio of $\mu = 0.41$. Two resolutions were considered, and the results showed a reasonable agreement between the trim parameters (cyclic and collective control inputs) computed versus those measured.

Then, the application of the method to the LES of an advancing helicopter rotor all the way to 30 diameters downstream was conducted. It has led to several insights into the vortex dynamics at play in the wake. In the near rotor region, the complex wake formation and roll-up processes (at least far more complex than those observed for fixed wing aircraft) were described, and the origin of the ensuing (self induced) turbulence development in the wake was identified. Vortex shedding from the dynamic stall occurring on the inboard part of the retreating blade is one of them. The interactions of tip vortices of different strength and orientation, mainly on the advancing side, is another feature favorable to the onset of turbulent conditions. Besides, through the help of 3D visualisations, the vortex dynamics involved in the generation of the two main wake vortices was qualitatively described: merging of blade tip vortices occuring on the advancing side, and reconnections on the retreating side.

From statistics gathered in transverse slices in the near and far wake regions, the emergence and the evolution of the two vortex system was also characterized in terms of integral quantities. Compared to an aircraft wake, it must be highlighted that, in the present simulation:

- the wake of the rotorcraft is not symmetric, and it has a maximum of vorticity on the advancing side;
- a growth in the 2D linear impulse (and hence on $\Gamma_0\, b_0$) of the main wake vortices was observed between 5 and 30 diameters behind the rotor;

- a fully developed turbulent wake was reached at 30 diameters, as suggested by the stabilization of Γ_0, b_0, and the ratio between the TKE and the total energy in the cross plane.

The second point was attributed to vortex stretching which was shown to align transverse vorticity in the streamwise direction. It is worth noticing that this feature is specific to helicopter wakes. In fact, the transverse vorticity involved in the alignment process is of course intrinsictly due to the blade tip vortices which are continuously shed over one revolution.

The approach presented here enables the identification and extraction of the far wake flow properties (circulation Γ_0, vortex spacing b_0) which, in turn, can be used in order to develop a physics-based wake model. Of course, further analyses should investigate the effect of rotor properties and operational conditions (tip speed ratio, number of blades, thrust coefficient, atmospheric turbulence, ground effect, etc.) on the far wake formation and decay.

In that respect, future simulations will explore the space of parameters mentioned, with further improvements of the rotor model. In particular, one expects that the inflow turbulence has a smaller influence on the decay process than what is observed for aircraft wakes, due here to the presence of strong self-induced turbulence which overwhelms the physics of the flow. The interaction of the rotor wake with the fuselage and the tail rotor, and with the wakes of these elements, should also be considered as a further source of wake perturbation.

Acknowledgements

D.-G. Caprace is supported by the Belgian french community F.R.S.-FNRS (Fonds de la Recherche Scientifique) under a PhD fellowship (Aspirant du F.R.S.-FNRS). The development work benefited from the computational resources provided by the supercomputing facilities of the Université catholique de Louvain (CISM/UCL) and the Consortium des Équipements de Calcul Intensif (CÉCI) en Fédération Wallonie Bruxelles (FWB) funded by the Fond de la Recherche Scientifique de Belgique (F.R.S.-FNRS) under Convention No. 2.5020.11. The production simulations used computational resources made available on the Tier-1 supercomputer of the FWB, infrastructure funded by the Walloon Region under the Grant Agreement No. 1117545.

References

[1] A. Reinke, S. Kauertz, T. Bauer, D. Fischenberg, F. Holzäpfel, D. Niedermeier, D. Vechtel, and C. Wolkensinger, "Aircraft wake vortex state-of-the-art & research needs," in *WakeNet3 Europe*, 2015.

[2] N. Matayoshi and Y. Okuno, "Evaluation of helicopter encounters with wake vortices," in *35th European Rotorcraft Forum*, 2009.

[3] Y. Wang, M. White, G. Barakos, P. Tormey, and P. Pantazopoulou, "Simulation of a light aircraft encountering a helicopter wake," *Journal of Aircraft*, vol. 52, no. 2, pp. 510–523, 2014.

[4] J. G. Leishman, M. J. Bhagwat, and A. Bagai, "Free-vortex filament methods for the analysis of helicopter rotor wakes," *Journal of aircraft*, vol. 39, no. 5, pp. 759–775, 2002.

[5] N. M. Komerath, M. J. Smith, and C. Tung, "A review of rotor wake physics and modeling," *Journal of the American Helicopter Society*, vol. 56, no. 2, pp. 22006–22006, 2011.

[6] N. M. Chaderjian and J. U. Ahmad, "Detached eddy simulation of the uh-60 rotor wake using adaptive mesh refinement," in *American Helicopter Society 68th Annual Forum*, (Texas), May 2012.

[7] R. E. Brown and A. J. Line, "Efficient high-resolution wake modeling using the vorticity transport equation," *AIAA journal*, vol. 43, no. 7, pp. 1434–1443, 2005.

[8] C. He and J. Zhao, "Modeling rotor wake dynamics with viscous vortex particle method," *AIAA journal*, vol. 47, no. 4, pp. 902–915, 2009.

[9] J.-f. Tan and H.-w. Wang, "Simulating unsteady aerodynamics of helicopter rotor with panel/viscous vortex particle method," *Aerospace Science and Technology*, vol. 30, no. 1, pp. 255–268, 2013.

[10] J. Zhao, C. He, L. Zhang, H. Zhao, and P. Hu, "Coupled viscous vortex particle method and unstructured computational fluid dynamics solver for rotorcraft aerodynamic interaction analysis," in *49th AIAA Aerospace Sciences Meeting*, vol. 1121, (Orlando, Florida), AIAA, 4-7 January 2011.

[11] N. Rajmohan, J. Zhao, C. He, J. Kim, L. Sankar, and J. Prasad, "An efficient pod based technique to model rotor/ship airwake interaction," in *68th American Helicopter Society Annual Forum*, (Fort Worth, Texas), 2012.

[12] C. He and N. Rajmohan, "Modeling the aerodynamic interaction of multiple rotor vehicles and compound rotorcraft with viscous vortex particle method," in *American Helicopter Society 72nd Annual Forum*, (West Palm Beach), May 17-19 2016.

[13] Y. Shi, Y. Xu, G. Xu, and P. Wei, "A coupling vwm/cfd/csd method for rotor airload prediction," *Chinese Journal of Aeronautics*, vol. 30, no. 1, pp. 204–215, 2017.

[14] P. Chatelain, M. Duponcheel, D.-G. Caprace, Y. Marichal, and G. Winckelmans, "Vortex particle-mesh simulations of vertical axis wind turbine flows: from the airfoil performance to the very far wake," *Wind Energy Science*, vol. 2, no. 1, p. 317, 2017.

[15] P. Chatelain, M. Duponcheel, S. Zeoli, S. Buffin, D.-G. Caprace, G. Winckelmans, and L. Bricteux, "Investigation of the effect of inflow turbulence on vertical axis wind turbine wakes," *Journal of Physics: Conference Series*, vol. 854, no. 1, p. 012011, 2017.

[16] B. Berry and I. Chopra, "Wind tunnel testing of an instrumented rotor at high advance ratio," in *56th AIAA/ASCE/AHS/ASC Structures, Structural Dynamics, and Materials Conference*, p. 0950, 2015.

[17] G. R. Whitehouse and A. H. Boschitsch, "Innovative grid-based vorticity–velocity solver for analysis of vorticity-dominated flows," *AIAA Journal*, vol. 53, no. 6, pp. 1655–1669, 2014.

[18] P. Chatelain, A. Curioni, M. Bergdorf, D. Rossinelli, W. Andreoni, and P. Koumoutsakos, "Billion vortex particle direct numerical simulations of aircraft wakes," *Computer Methods in Applied Mechanics and Engineering*, vol. 197, pp. 1296–1304, Feb 2008.

[19] R. Cocle, G. Winckelmans, and G. Daeninck, "Combining the vortex-in-cell and parallel fast multipole methods for efficient domain decomposition simulations," *Journal of Computational Physics*, vol. 227, pp. 9091–9120, Nov 2008.

[20] P. Chatelain and P. Koumoutsakos, "A Fourier-based elliptic solver for vortical flows with periodic and unbounded directions," *Journal of Computational Physics*, vol. 229, pp. 2425–2431, 4 2010.

[21] I. F. Sbalzarini, J. H. Walther, M. Bergdorf, S. E. Hieber, E. M. Kotsalis, and P. Koumoutsakos, "PPM a highly efficient parallel particle mesh library for the simulation of continuum systems," *J. Comput. Phys.*, vol. 215, pp. 566–588, July 2006.

[22] G. S. Winckelmans, *Encyclopedia of Computational Mechanics*, ch. Vortex Methods, pp. 129–153. John Wiley & Sons, Ltd, 2004.

[23] S. Backaert, P. Chatelain, and G. Winckelmans, "Vortex particle-mesh with immersed lifting lines for aerospace and wind engineering," in *Symposium on Particle Methods in Fluid Dynamics* (J. H. Walther, ed.), vol. 18 of *Procedia IUTAM*, (DTU Copenhagen), pp. 1–7, IUTAM, October 2012.

[24] E. Dyachuk, A. Goude, and H. Bernhoff, "Dynamic stall modeling for the conditions of vertical axis wind turbines," *AIAA journal*, vol. 52, no. 1, pp. 72–81, 2013.

[25] J. N. Sørensen, R. F. Mikkelsen, D. S. Henningson, S. Ivanell, S. Sarmast, and S. J. Andersen, "Simulation of wind turbine wakes using the actuator line technique," *Proceedings of the Royal Society of London. Series A, Mathematical and Physical Sciences*, vol. 373, no. 2035, 2015.

[26] N. Docquier, A. Poncelet, and P. Fisette, "Robotran: a powerful symbolic gnerator of multibody models," *Mechanical Sciences*, vol. 4, no. 1, pp. 199–219, 2013.

[27] G. M. Bowen-Davies, *Performance and Loads of Variable Tip Speed Rotorcraft at High Advance Ratios*. PhD thesis, University of Maryland, College Park, 2015.

[28] A. H. Lind and A. R. Jones, "Unsteady airloads on static airfoils through high angles of attack and in reverse flow," *Journal of Fluids and Structures*, vol. 63, pp. 259–279, 2016.

[29] G. Bir, I. Chopra, and K. Nguyen, "Development of umarc (university of maryland advanced rotorcraft code)," in *American Helicopter Society 46th Annual Forum*, 1990.

[30] K. S. Wittmer, W. J. Devenport, M. C. Rife, and S. A. Glegg, "Perpendicular blade vortex interaction," *AIAA journal*, vol. 33, no. 9, pp. 1667–1674, 1995.

[31] D. Reich, S. Willits, and S. Schmitz, "Scaling and configuration effects on helicopter rotor hub interactional aerodynamics," *Journal of Aircraft*, 2017.

[32] I. De Visscher, *Interaction of wake vortices with the atmosphere and the ground : advanced numerical simulation and operational modeling*. PhD thesis, Université catholique de Louvain, 2012.